Volume 1 | Number 1 | Jan 2013 | Pages 1–100

Journal of
Materials Chemistry C

Materials for optical and electronic devices
www.rsc.org/materialsC

ROYAL SOCIETY
OF CHEMISTRY

ROYAL SOCIETY
OF CHEMISTRY

www.rsc.org/materialsC

Journal Name

ARTICLE

Optical and structural properties of Nd doped SnO₂ powder fabricated by the sol-gel method

K. Bouras,[a] J.-L. Rehspringer,[b] G. Schmerber,[b] H. Rinnert,[c] S. Colis, G. Ferblantier,[a] M. Balestrieri,[b] D. Ihiawakrim,[b] A. Dinia[b] and A. Slaoui[a].

We report on the structural and optical properties of undoped and neodymium doped SnO₂ powders (0, 1, 3, and 5 at% of Nd) synthesized by the sol-gel method. SEM and TEM microscopies reveal a nanometric scale of the powders. We show that the tetragonal rutile phase is achieved after annealing at 700°C. The crystallites size of the doped SnO₂ is found to decrease gradually with the increase of Nd content without changing the SnO₂ structure. A strong decrease in the intensity of the Raman peaks is noted for doped powders, which can be attributed to the location of Nd³⁺ ions at the Sn sites indicating Nd incorporation in the host matrix. For the first time the optical properties were studied by UV-Vis-NIR spectroscopy and revealed Nd related absorption bands in the SnO₂ matrix. The investigation of the photoluminescence properties shows a broad emission centred around 550-650 nm originating from defects present in the SnO₂ host matrix. Under 325 nm laser excitation, a strong photoluminescence of trivalent Nd is observed in the infrared region and shows Nd related emission peaks at 885, 1065, 1336 nm. Such strong PL signal under laser excitation indicates that Nd³⁺ is optically active. The excitation dependent PL (PLE) recorded in the 450-700 nm range confirms the presence of active Nd³⁺ successfully inserted into the SnO₂ host matrix.

Introduction

Tin dioxide (SnO₂) is one of the most attractive materials studied over the last decade due to its several applications in optical technologies, optoelectronic devices, gas sensors,[1, 2] solar cells and lithium ion batteries.[3, 4] Its optical and electrical properties are linked to its crystallographic structure. SnO₂ possesses a wide optical band gap[5] (around 3.6 eV for bulk material at room temperature) and its crystalline structure is known to be tetragonal rutile–type. It exhibits n-type conductivity due to the interstitial tin atoms and oxygen vacancies,[6] which act as donors in the host matrix.[7] The wide band gap of tin dioxide leads to a decrease of luminescence quenching effects and to a higher excitonic ionization energy.[8] SnO₂ presents also a high transparency in the visible range along with a strong reflectivity in the infrared region,[9] and has remarkable chemical and thermal stabilities in atmospheric environment.[10] Such features can be strongly tuned for nanostructured SnO₂.

Considerable work has been reported on synthesis of nanostructured SnO₂. A vast selection of morphologies can be obtained, such as nanorods,[1, 11, 12] nanosheets,[13] nanowires,[14] nanoflakes core-branched nanoarrays,[15] nanoribbons[16] and nanocrystals,[17, 18] which explore novel properties. In particular, SnO₂ powder can be easily synthesized through different chemical methods, such as co-precipitation,[19, 20] hydrothermal[21, 22] and sol-gel.[23, 24] The final

properties of tin dioxide nanostructures are related to both the composition and the processing method.

On the other hand, the combination of the rare-earth ions with wide band gap semiconductors is considered as part of a new class of materials[25] that have a high potential for the production of several optical devices such as fiber amplifiers, lasers, fluorescent lamps, optical memories, LCD and field emission displays, in telecommunications (long-haul and local area networks) and interconnects.[25, 26] In particular, interest in the physical properties of tin dioxide has significantly increased recently, especially when it is doped with rare earth elements (Ce, Nd, Sm, Eu, Er, Yb …).[6, 27-30] In fact, due to its high transparency in the visible range, SnO₂ is an interesting host for the incorporation of luminescent rare earth ions providing emission from the visible to the infrared regions.[29] Interestingly, these ions can functionalize the host with valuable photon converting properties thanks to the 4f shell transitions.[31] Rinnert et al.[32] have reported on evaporated Nd doped SnO₂ thin films for their use as optical converter. Also, Nd doped SnO₂ powder has been studied by Wu et al.[21] for gas sensing applications.

In this work, we report for the first time on the structural and optical properties of undoped and Nd doped SnO₂ powders prepared by the sol-gel process and thermally annealed at 700°C. We investigate the incorporation of Nd atoms into the SnO₂ matrix and the consequence on the optical properties of the Nd:SnO₂ powders. We discuss also

the possibility of an energy transfer occurring between the host SnO_2 and the rare earth element (Nd) versus the Nd concentration.

Experimental

Synthesis. Undoped and Nd doped SnO_2 as $[SnO_2]_{1-x}Nd_x$ solutions are provided by RBnano[33] where x was set to 0, 1, 3% and 5 at %. It consists of metal-organic tin precursor in solution in propionic acid (product RBnano RBN119). For doping, Nd is added in the previous solution as neodymium (III) acetate hydrate 99.9% (Alfa Aesar). The sol-gel solutions were then annealed at 700°C for 3h in air in order to get SnO_2 crystallization. Small crystals were obtained and further thoroughly ground in an agate mortar to obtain a fine powder. In the following, the samples will be labelled SnO_2 and SnO_2:Nd x with x =1, 3 and 5%.

Characterizations. The morphology and particles size were determined by using a JEOL 6700F scanning electron microscope (SEM) while the crystallites size and the degree of crystallinity of these powders were extracted from X-ray diffraction (XRD) measurements and Raman spectroscopy, respectively. The powders were examined using a Siemens D5000® X-ray diffractometer equipped with a monochromatic Cu $K\alpha_1$ incident radiation in the 2θ range of 10°-80° (λ=0.154056 nm). Additional information on the crystalline structure was obtained by TEM observations carried out on a JEOL JEM2100, 200KV microscope with a resolution of 0.23 nm. Raman spectra were obtained using a confocal dispersive Raman microprobe-LabRam Aramis from Horiba Jobin-Yvon Co. equipped with a YAG (λ = 532 nm) laser as an excitation source. The power was minimized to 9 mW to avoid any deformation of the structure due to laser heating. The spectrometer resolution is lower than 1 cm^{-1} and the data were collected in the 250-1000 cm^{-1} range. The optical properties were investigated using an ultraviolet-visible-near infrared (UV-visible-NIR) Perkin-Elmer Lambda 950 spectrophotometer. Finally, the emission properties of the luminescent material were investigated at room temperature using a He-Cd laser at a wavelength of 325 nm. In order to avoid powder degradation, the applied power was chosen to 10 mW. For the photoluminescence (PL) measurements in the 350-950 nm range, the signals were recorded by means of a cooled CCD camera. The acquisition time was varied from 10 to 20 s. In the 800-1500 nm range, the signal was analyzed by a monochromator equipped with a 600 grooves/nm grating and by an InP/InGAs photomultiplier tube cooled at 190 K.

Results and discussion

Structural properties of SnO_2 and $Nd-SnO_2$ powders. Scanning Electron Microscopy (SEM) analysis has been carried out to examine the morphology and the grains size of the synthesized powders. The observations are shown in Figure 1 for the pure SnO_2 and Nd doped powders. Worth noting that all powders consist of nano-aggregated round shaped grains, with a regular, similar and homogenous distribution. No impurities were observed and no Nd-

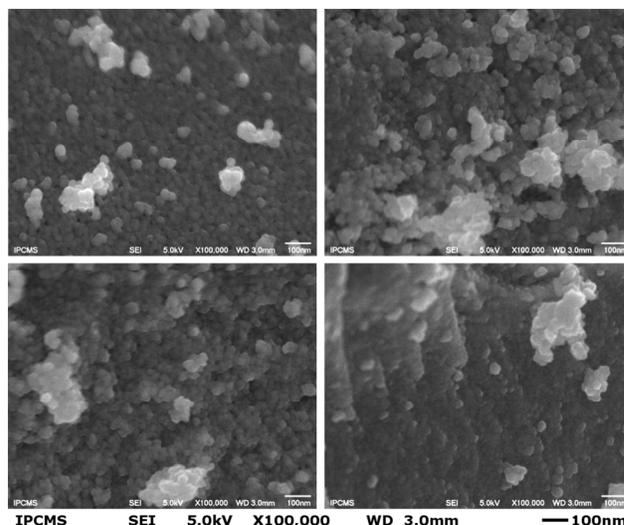oxide compounds were revealed in the detection limit of our compositional analysis.

Fig. 1 SEM images of (a) SnO_2, (b) SnO_2:Nd 1%, (c) SnO_2:Nd 3% and (d) SnO_2:Nd 5 %

EDS (Energy-Dispersive X-ray Spectroscopy) analysis was used to determine the Nd content present in the doped powders. The extracted data are reported in table 1. It is found that the measured Nd concentrations are in good agreement with the nominal values, the deviation being about 15 %.

Element	Nd concentration (%)
SnO_2:Nd 1%	1.09 % ± 0.43
SnO_2:Nd 3%	2.45 % ± 0.41
SnO_2:Nd 5%	4.43 % ± 0.38

Table. 1 The chemical composition of the Nd doped SnO_2 powders as estimated from EDS analysis.

To get a more precise estimate of the particles size in our materials, we examined the powders at a smaller scale using transmission electron microscopy (TEM). The bright field images of the undoped and Nd 3% doped SnO_2 are shown in Figures 2a and 2d. It is clearly seen that the powders are composed of agglomerated nanometric particles. The nanoparticles size is in the range of 14-24 nm with an average of about 20 nm for the undoped powder while for the Nd-doped one, the mean size is of about 9 ± 2 nm. The data for all Nd-doped samples are reported in Table 2. The particles size distribution was extracted from TEM measurements for undoped and all Nd-doped SnO2 powders. The results are displayed in Figure 3, which confirms clearly the decrease of the particles size with the adding of more Nd in the SnO2 matrix. This indicates a possible insertion of Nd into the matrix. The TEM images also show the presence of Moiré fringes suggesting a well-defined crystallization of the particles. For a better view, high-resolution images were recorded and shown in figures 2b and 2e for the undoped and Nd 3% doped SnO_2, respectively. It can be clearly seen from the HRTEM images

that the atomic planes are well defined. Moreover, the lattice parameter 'a' can be deduced from the (110) interplane distance and is estimated to be $3{,}35 \pm 0{,}05$ Å and $3{,}37 \pm 0{,}05$ Å for the undoped and doped SnO_2, respectively. This increase in the lattice parameter suggests an increase of the unit cell volume for the doped powder, which can be considered as a second proof of Nd insertion in the host matrix
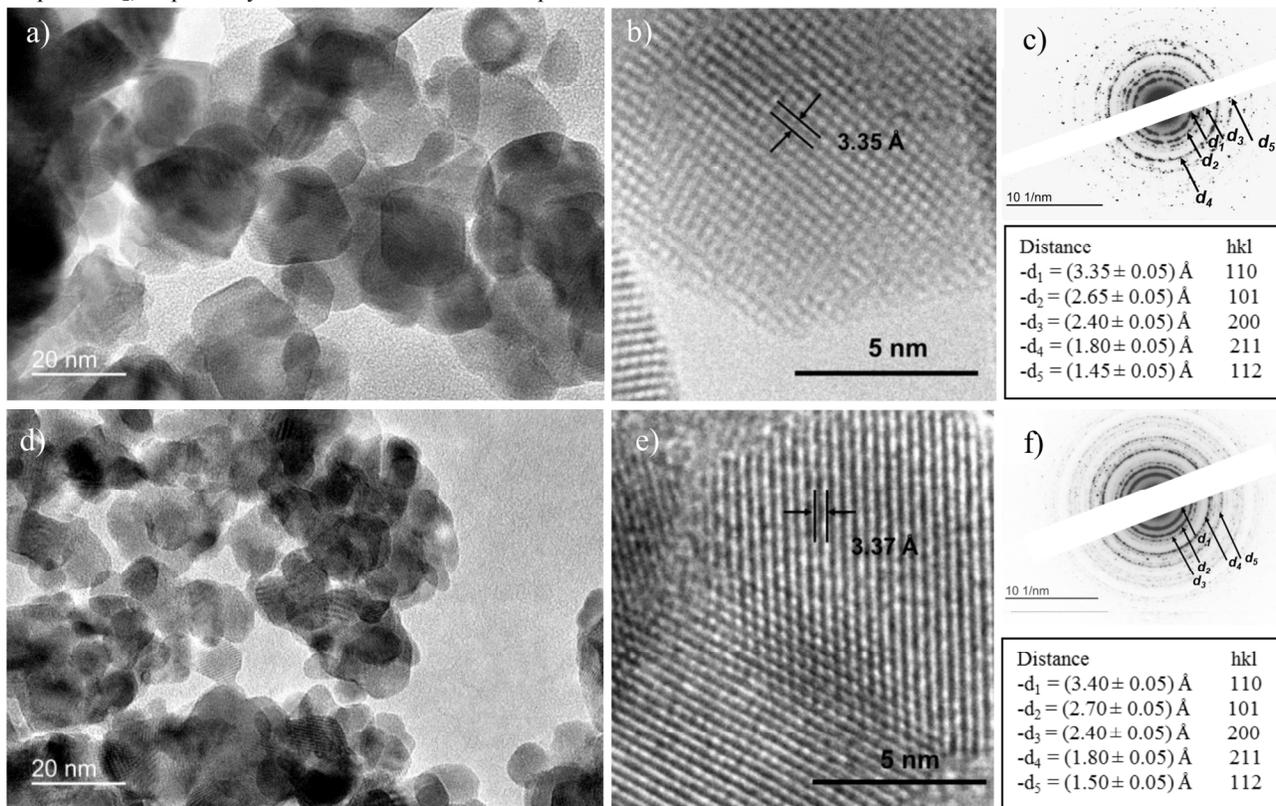

Fig. 2 TEM, HRTEM images and SAED patterns of undoped (a, b and c) and 3% Nd doped SnO_2 (d, e and f) powders respectively.

To get better insights on the crystallinity of the synthesized powders, we first checked the crystallinity of the nanoparticles (at a small range) using selected area electron diffraction (SAED) observations. The images are presented in figures 2c and 2f for the undoped and SnO_2: Nd 3% samples respectively. The patterns show circular rings characteristic of polycrystalline samples; all rings can be indexed in the rutile phase. The tables below each SAED pattern give the d_{hkl} of the most intense orientations, and reveal a significant distance shift for the doped powder. This shift can be attributed to the Nd insertion. The diffraction rings are also more continuous for the doped sample (fig. 2d), suggesting a better statistic (and therefore smaller crystallites) with respect to undoped SnO_2. EDS measurements were also performed during the TEM analysis (not shown here) and have confirmed the concentrations reported in Table 1 as determined by SEM-EDS analysis.
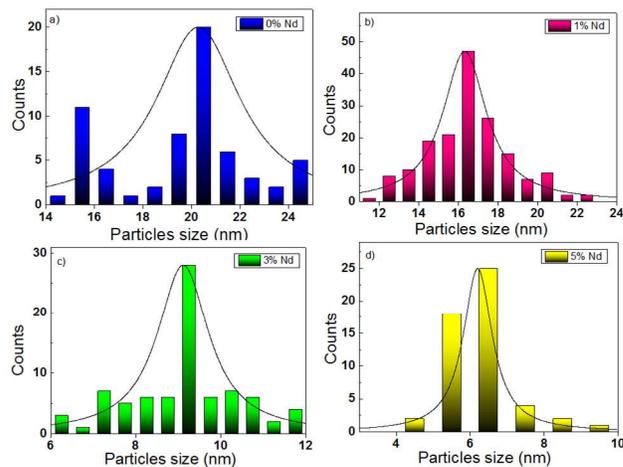

Fig. 3 Nanoparticles size distribution of SnO_2 (a), SnO_2:Nd 1% (b), SnO_2:Nd 3% (c), SnO_2:Nd 5% (d) powders.

In the section above, the structural analyses of the synthesized powders were performed at a very small range and have therefore a local character. For this reason, the structural properties of the powders were also investigated at a larger scale using X-ray diffraction (XRD). Figure 4a shows the X-ray diffraction patterns for

SnO_2:Nd	0% Nd	1% Nd	3% Nd	5% Nd
Mean size (nm)	20 ± 4	16 ± 3	9 ± 2	6 ± 2
Range (nm)	14-24	12-22	6-12	4-10

Table. 2 The average nanoparticles size of SnO2 versus Nd concenration in the matrix.

SnO$_2$:Nd powders with Nd concentrations of 0, 1, 3, and 5%. All diffraction peaks can be assigned to the tetragonal rutile phase of SnO$_2$ (reference card JCPDS 00-041-1445 of ICDD).
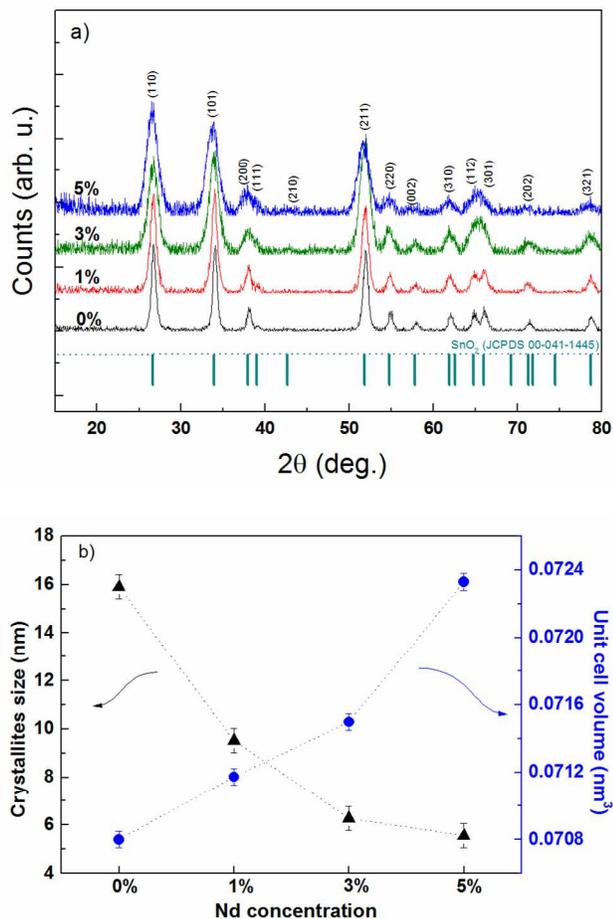

Fig. 4 a) X-ray diffraction patterns of Nd-doped SnO$_2$ powders with Nd concentration (0, 1, 3 and 5 %). Vertical bars correspond to SnO$_2$ JCPDS card n° 00-041-1445, b) Dependence of the crystallites size of SnO$_2$:Nd powders and the unit cell volume as a function of Nd-doping.

Moreover, it can be noted that the Nd doping does not affect the tetragonal structure of SnO$_2$ and no secondary phases such as SnO or Nd$_2$O$_3$ are detected in the limit of the XRD technique. This is in agreement with SEM and TEM observations which showed a homogeneous distribution of Nd within the samples.
With increasing Nd content, a slight peak shift towards lower angles is observed, which agrees with SAED analysis. This suggests an increase of the lattice parameter due to tensile/compressive stress on the lattice. This is mainly due to the rare earth incorporation and less to the presence of defects.
On the other hand, the full-width at half maximum (FWHM) of SnO$_2$:Nd x% peaks increases as the Nd content increases indicating that the average crystallites size decreases gradually with increasing Nd content. This is in accordance with the TEM results reported above.

The average crystallites size of the SnO$_2$:Nd powders is usually determined using the Scherrer formula:[34] $= 0.9 \ / \ \cos(\ )$,

where λ is the X-ray wavelength, β is the FWHM of the (h k l) peaks and θ is the Bragg angle. Only (110), (101) and (211) peaks were introduced into the calculations. Figure 4b shows that the average crystallites size decreases gradually as the Nd concentration increases. The average crystallites size is found about 16 nm for the undoped SnO$_2$ and decreased down to 5 nm for the 5% Nd doped SnO$_2$ powder. The unit cell volume plotted also in Figure 4b is calculated using both the relation $= 1/\sqrt{(h^2 + h^2)/ \ ^2 + \ ^2/ \ ^2}$ and the Bragg law. We found that the unit cell volume is an increasing function of the Nd concentration which indicates that some Nd atoms substitute Sn atoms in the host matrix. Since the ionic radius of the Nd^{3+} (0.11 nm) is larger than the ionic radius of Sn^{4+} (0.069 nm), incorporating Nd^{3+} ions into the matrix leads most likely to some distortion and stress in the cell and the lattice respectively. As a consequence, the grains might break which causes a decrease in the crystallites size with respect to the Nd addition.

To further investigate the crystalline structure and follow structural changes induced by Nd doping, Raman spectroscopy measurements for all powders were performed. Figure 5 shows the Raman spectra of the undoped and Nd-doped SnO$_2$ powders. Some optical modes are observed, namely the three fundamental peaks at 475, 632, and 775 cm^{-1} assigned to E$_g$, A$_{1g}$, B$_{2g}$ respectively[35, 36] and the three weak peaks at 249, 302, and 355 cm^{-1} to be assigned to the E$_u$(2) TO, E$_u$(2) LO, and E$_u$ LO modes respectively. The other peaks at 143, 504, 554, and 692 cm^{-1} are attributed to B$_{1g}$, B$_{1u}$ (2), B$_{1u}$ (3), and A$_{2u}$ LO modes, respectively[1, 35, 37] Thus, the Raman spectra confirm the presence of the rutile phase[38-40] which belongs to the space group $^{14}_{4h}$, P42/mnm with 2 molecules per unit cell and characterized by the presence of the four Raman active modes, namely B$_{1g}$, E$_g$, A$_{1g}$, and B$_{2g}$. In fact the optical modes are represented as follows:

$$\Gamma = A_{1g} + A_{2g} + B_{1g} + B_{2g} + E_g + A_{2u} + 2B_{1u} + 3E_u$$

where the A$_{2g}$ and 2B$_{1u}$ modes are neither Raman active nor infrared (IR) active, while the A$_{2u}$ and E$_u$ modes are IR active, and the remaining A$_{1g}$, B$_{1g}$, B$_{2g}$, and E$_g$ modes are Raman active.[41]
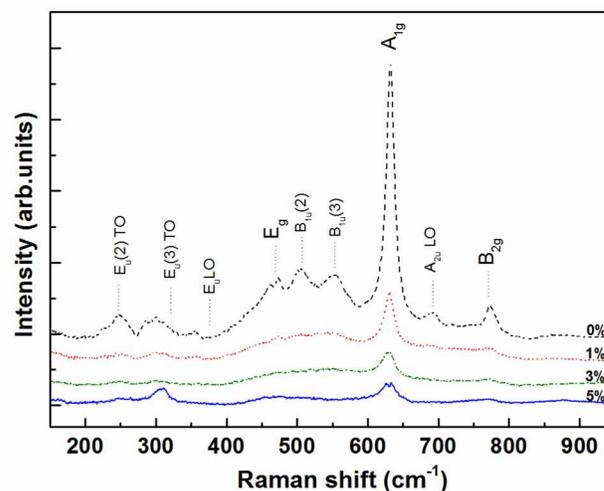
Fig. 5 Raman spectra of SnO_2: Nd powders with different Nd concentrations (0, 1, 3 and 5%).

Figure. 5 indicates that the addition of Nd in the host matrix induces major changes in the Raman spectra features. The intensities of the three fundamental vibrational peaks (E_g, A_{1g}, and B_{2g}) and of the B_{1u} mode are found to decrease as the Nd content increases. On the other hand, the other peaks corresponding to the inactive Raman modes (A_{2u} and E_u) disappeared which suggests Nd incorporation in the SnO_2 lattice and therefore confirms the TEM and XRD results.

Optical properties of the SnO_2 and Nd-SnO_2 powders. We demonstrated above that Nd is successfully inserted into the SnO_2 host matrix by studying the structural properties. In the following, we will discuss the effect of Nd doping on the optical properties of the synthesized SnO_2 powders. Figure 6 plots the UV-visible-NIR absorption spectra of the undoped and Nd doped SnO_2 powders recorded in the 250-1000 nm range. The undoped powder shows a strong absorption in both UV-blue ranges of the spectrum and NIR region. In the UV-blue part, no abrupt absorption is observed, but a slope extending over 200 nm. The spectra exhibit a considerable absorption in the 250-550 nm wavelength range and an absorption edge from 300 to 480 nm due the large exciton binding energy. These observations are in good agreement with those reported by Bouaine et al.[19] and are expected for SnO_2.

While no features are observed for the undoped SnO_2 sample, the doped powders spectra exhibit Nd related absorption peaks at 513, 524, 583, 680, 744, 802 and 872 nm. These observations will help understanding the excitation mechanisms of the Nd^{3+} ions that will be discussed in the photoluminescence section below. All these peaks correspond to direct excitation of electrons from the $^4I_{9/2}$ ground state to upper excited states by comparing with the electronic level configuration of Nd^{3+} in $LaCl_3$: Nd crystals[25, 42, 43] presented in figure 10. Such a result is particularly important for applications such as solar cells for which SnO_2 is used as a transparent conducting oxide (TCO).
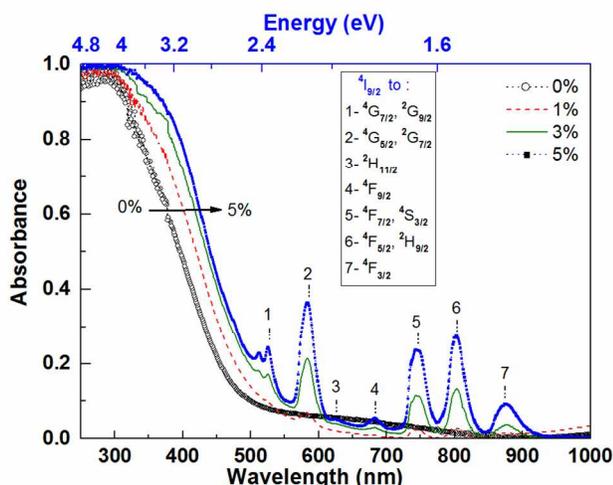

Fig. 6 Absorbance spectra of Nd-doped SnO_2 powders versus Nd content.

The figure 6 reveals a significant shift of the absorption edge towards lower energies by increasing the Nd content. We have avoided the extraction of the band gap of our materials from these curves because the character of the SnO_2 band gap is still highly controversial. Some authors assume an indirect transition,[44] while many others suggest a direct transition across the gap.[5, 45, 46] In all cases, the data suggest a decrease in the band gap with Nd addition, which is in favour of Nd insertion into the SnO_2 matrix. Our conclusion is that the absorption threshold of the Nd doped powders enhances with the Nd content.

Luminescence properties of the SnO_2 and Nd-SnO_2 powders. As discussed before, the Nd doping induces noticeable structural and optical changes on the SnO_2 matrix which are expected to affect the luminescence properties of the powders.

Figure 7 shows the UV-Vis-NIR emission spectra of pure SnO_2 and doped SnO_2:Nd 5% powders recorded under a 325 nm (3.81 eV) laser excitation. These spectra cover a large part of the spectral range useful for applications such as solar cells.

Since the gap energy of the pure SnO_2 powder is about 3.6 eV, the band to band emission should appear at about 344 nm. This emission is however not observed in the PL spectrum because of the detection limit of our PL setup. However, the pure SnO_2 powder exhibits a very strong luminescence band centered at 600 nm, and a much less intense one in the 400-450 nm region.
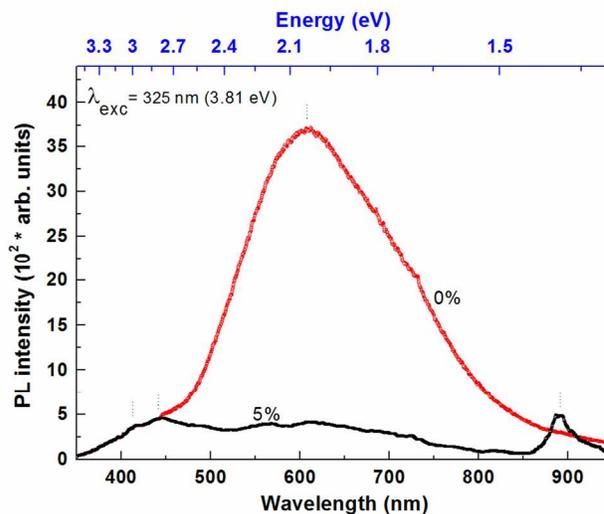

Fig. 7 Room temperature emission spectra of undoped and 5% Nd doped SnO_2 powders

The large and intense band around 600 nm can be attributed to the presence of deep levels in the bandgap of SnO_2[16] whose the origin can be multiple. It is generally admitted that oxygen vacancies, which are present at a high concentration in oxide based powders, can lead to the formation of important amount of trapped states within the band gap. In particular, oxygen vacancies are one of the dominant defects that form donor levels, which usually play an important role in the PL process.[27, 46, 47] Another source of luminescence centers in SnO_2 materials can be the presence of tin interstitial atoms resulting from the preparation technique. The large amount of grains boundaries in the powder can also induce efficient recombining luminescent centers. Similar observations in quantum nanoparticles systems have been reported in the literature.[47-49]

As for the band in the 400-450 nm range, earlier studies have shown a broad dominant peak near 396 nm (about 3.14 eV). Gu et al.[27] have

already reported the presence of peaks centered at around 414 and 440 nm. The peak at 414 nm was assigned to the electron transitions from the donor levels created by oxygen vacancies to the valence band,[24] while the peak at 440 nm can be ascribed to the luminescent centers due to inter-grains defects.[39]

Figure 7 displays also the PL spectrum of the highly doped 5% Nd:SnO$_2$ powder. The two peaks in the UV region are again present and exhibit comparable PL intensities than for the undoped SnO$_2$ sample. In contrast, the band in the visible region is almost 10 times weaker than that for pure SnO$_2$. This result indicates that the presence of Nd induces fundamental changes in the defects type and density, and consequently influences the radiative recombination processes. This also could mean that the non-radiative recombinations (such as point defects, dislocations, surface/interface states, and grain boundary states) are increased with the presence of Nd^{3+} ions. Another possibility supported by the XRD analysis is that considerable amount of Nd atoms substitutes Sn atoms in the host matrix. This observation does not exclude the presence of Nd atoms in interstitials sites, which can compensate defects related to the oxygen vacancies.

Figure 7 shows that the strong decrease of PL band in the visible range is accompanied by an emission line centred at 885 nm and usually attributed to the $^4F_{3/2} \Rightarrow{} ^4I_{13/2}$ transitions of Nd^{3+}. A second, less intense band appears around 820 nm. This is a good indication that Nd is inserted in the SnO$_2$ matrix and optically active. In fact, inserted Nd atoms in the SnO$_2$ matrix induce simultaneously a strong effect on the defects responsible of the PL in the visible region, and a light emission in the NIR region (radiative recombination process). At a first glance, the observed behaviour can suggest that an energy transfer occurs from the SnO$_2$ band to Nd^{3+}. Similar conclusions were drawn for Nd doped ZnO nanocrystals[50] and Nd doped SnO$_2$ thin films.[32]

To highlight the role of Nd in a possible transfer process, we have recorded the photoluminescence for all synthesized Nd doped SnO$_2$ powders. The emission patterns of the powders having different Nd concentrations (1, 3, and 5%) are shown in Figure 8.
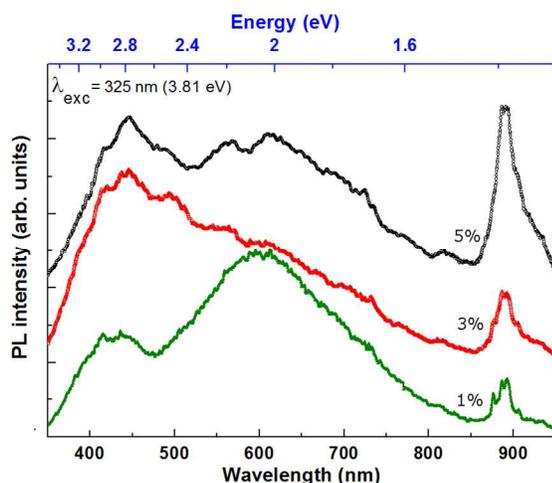

Fig.8 Room temperature UV-to-NIR emission spectra of Nd doped SnO$_2$ powders with different Nd content. (An offset has been introduced in order to improve clarity)

It is interesting to note that, while the shape of the two defect emission bands does not present major changes, the intensity of the peaks is very sensitive to the Nd content in the SnO$_2$ powder. This is especially the case for the NIR emission intensity which increases with the Nd concentration thanks to more Nd elements in the powder.

Since Nd^{3+} is expected to emit further in the NIR region, additional PL measurements have been performed to have a closer look to the Nd emission using a better resolved and longer wavelength range detector. The PL between 850-1200 nm under He-Cd laser excitation is reported in Figure 9. Three emission groups can be observed. The first peaks are those reported in figure 7, centred at 885 nm, while two more groups appear at 1065 and 1336 nm. These peaks are commonly assigned to the $^4F_{3/2} \Rightarrow{} ^4I_{n/2}$ transitions, with n equal to 13, 11 and 9, respectively[32]. The intensity of these emission groups enhances with Nd addition. No quenching effect was observed meaning that most of the Nd atoms are incorporated into SnO$_2$. To explain the PL lines and discuss the possibility of an energy transfer in our Nd doped systems, we represent in Figure 10 the energy levels diagram of SnO$_2$ and Nd^{3+} ions, to clarify the possible transitions.
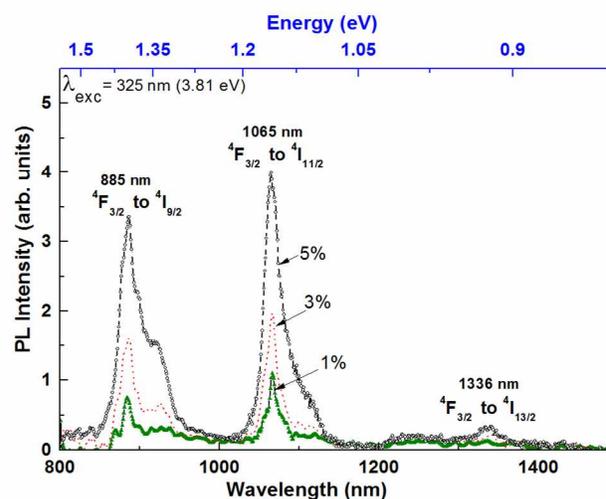

Fig.9 Room temperature IR emission spectra of Nd doped SnO$_2$ powders with different Nd content.

Since the excitation wavelength for PL measurements is 325 nm (3.8 eV, superior to the band gap of our doped powders), the excitation of the Nd^{3+} ions might occur via indirect mechanisms. As a first process, (i) the band to band transition of the host SnO$_2$ can transfer all the energy (3.6 eV) to the 4f electrons of Nd^{3+}. Another possible energy transfer process is that occurring via transitions throughout the electron trapped states within the band gap (ii), (iii) and (iv). These two cases represent the resonant energy transfer process in the ideal case. These processes are schematically drawn in Figure 10.

Concerning the process involving the traps, it can be speculated that photons emitted between 500 and 800 nm (process involving traps in SnO$_2$) can be appropriate to excite the Nd^{3+} ions from the ground state $^4I_{9/2}$ to the $^4G_{5/2}$, $^2F_{7/2}$ excited states. As a matter of fact, we have shown in figure 6 that the SnO$_2$ powders absorb light in the visible region, in particular around 600 nm, which corresponds also to the

main emission region of SnO$_2$. The desexcitation of the Nd^{3+} ions to the ground state will result into the three well resolved peaks reported above. In other words, the absorption band of SnO$_2$ in the visible region provide a sensitizing band to excite the Nd^{3+} ions, which then relaxes by emitting NIR photons.
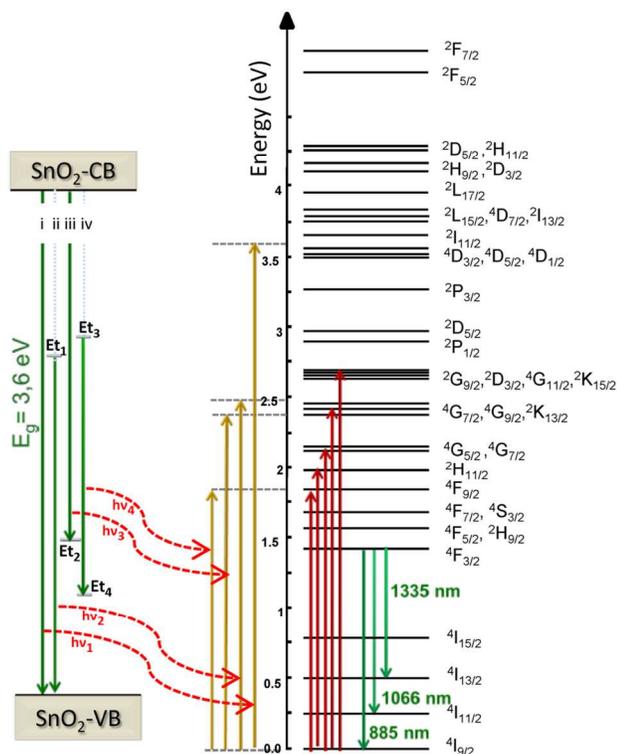

Fig.10 Energy levels diagram of the Nd^{3+} ions observed in LaCl$_3$[42, 43], and the process of potential energy transfer from SnO$_2$ to Nd^{3+}.

For deeper investigation on a possible indirect excitation process, photoluminescence excitation (PLE) spectroscopy experiments were carried out on the Nd doped powders. Figure 11 plots the PLE spectrum of the SnO$_2$:Nd 3% powder recorded by monitoring the near-infrared (NIR) $^4F_{3/2}$ ➔ $^4I_{11/2}$ emission at 1066 nm in the 450-700 nm range. The PLE was performed at room temperature using an optical parametric oscillator (OPO) laser. The average laser power was around 30 mW.

The PLE spectrum exhibits Nd^{3+} excitation lines centred at 470, 530, 585 and 611, 628 and 685 nm which correspond to the direct excitation of electrons from the ground state $^4I_{9/2}$ of Nd^{3+} to the upper excited states $^2G_{9/2}$, $^4G_{11/2}$ and $^4G_{9/2}$, $^4G_{7/2}$ and $^4G_{5/2}$, $^2G_{7/2}$, and $^2H_{11/2}$ and $^4F_{9/2}$ respectively (see fig. 10). It is interesting to notice the increase of the background of the spectrum when excitation is increased towards higher energies (represented by the dashed line in fig. 11).

The fact that the increase of background occurs in a region where the SnO$_2$ matrix absorbs can indicate that some transfer occurs through

one of the mechanisms described in figure 10. The absorbance of SnO$_2$:Nd 3% is also reported for comparison
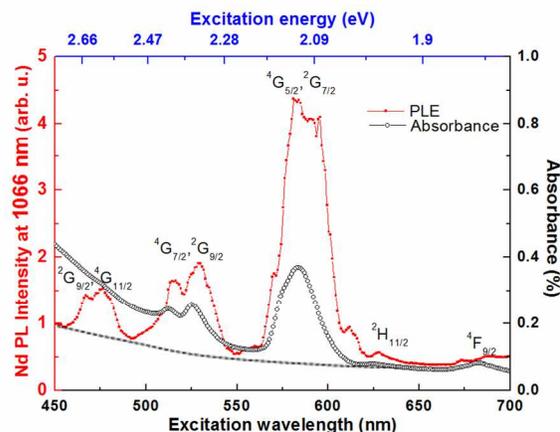

Fig. 11 PLE spectrum at 1066 nm for the 3% Nd doped SnO$_2$ powder

The overlap between the absorption of the SnO$_2$ matrix and the different energy levels of Nd^{3+} ions is favourable to the energy transfer process. However, it is difficult to quantify the real efficiency of such process. Further studies are needed to estimate the energy transfer efficiency.

Conclusions

Undoped SnO$_2$ and Nd doped SnO$_2$ (Nd:SnO$_2$) powders were synthesized by the sol-gel method and annealed at 700°C. SEM observations indicate a high agglomeration factor at a macroscopic level, and a uniform distribution of the particles size. TEM images showed that the particles size is decreasing with increasing Nd content. The crystallinity, structure and crystallites size for the powders were determined by XRD and SAED measurements. A tetragonal crystalline phase is demonstrated for all samples. A slight diffraction angle shift to lower angles is observed with increasing Nd content, indicating effective Nd incorporation. The insertion of Nd atoms in the host matrix as well as the crystallinity of the grains in the powder was also confirmed by Raman spectroscopy analysis.

On the other hand, the absorption energy threshold was found to be lower for the Nd doped SnO$_2$ powders as compared to the undoped one. We also evidenced for the first time Nd related absorption bands in the visible region in SnO$_2$ matrix.

Finally, photoluminescence measurements of synthesized powders demonstrated the activation of the rare earth element in the matrix. Thus, strong photoluminescence features in the near infrared region were observed as a consequence of the desexcitation from the high energy states of the Nd^{3+} ions to the background state. The PLE spectroscopy was applied to investigate direct and indirect excitations mechanisms of the Nd^{3+} ions. Some evidence for the energy transfer from the SnO$_2$ matrix to Nd was demonstrated but further studies are needed to confirm the process for the Nd doped SnO$_2$ systems. Nevertheless, these results are already very encouraging for the implementation of thin films of Nd doped SnO$_2$

as photon down shifter layers for optoelectronic devices such as solar cells.

Notes and references

a ICube, Université de Strasbourg-CNRS UMR 7163, 23 rue du Loess, BP 20 CR, 67037 Strasbourg Cedex 2, France

b IPCMS, Université de Strasbourg-CNRS, UMR 7504, 23 rue du Loess, BP 43, 67034 Strasbourg Cedex 2, France

c IJL, Université de Lorraine-CNRS, UMR 7198, Boulevard des Aiguillettes, BP 70239, 54506 Vandœuvre-lès-Nancy, France

1. Y. J. Chen, L. Nie, X. Y. Xue, Y. G. Wang and T. H. Wang, *Appl. Phys. Lett.*, 2006, **88**, 083105.
2. M. Kumar, A. Kumar and A. C. Abhyankar, *Ceram. int.*, 2014, **40**, 8411-8418.
3. J. S. Chen and X. W. Lou, *Small*, 2013, **9**, 1877-1893.
4. Y. Idota, T. Kubota, A. Matsufuji, Y. Maekawa and T. Miyasaka, *Science*, 1997, **276**, 1395-1397.
5. F. J. Arlinghaus, *Journal of Physics and Chemistry of Solids*, 1974, **35**, 931-935.
6. E. A. Morais, L. V. A. Scalvi, L. P. Ravaro, S. M. Li and E. A. Floriano, *J. Phys. Conf. Ser.*, 2010, **249**.
7. J. Jeong, S.-P. Choi, C. I. Chang, D. C. Shin, J. S. Park, B. T. Lee, Y.-J. Park and H.-J. Song, *Solid. State. Commun.*, 2003, **127**, 595-597.
8. P. N. Favennec, H. L'Haridon, M. Salvi, D. Moutonnet and Y. Le Guillou, *Electronics Letters*, 1989, **25**, 718-719.
9. M. Batzill and U. Diebold, *Prog. Surf. Sci.*, 2005, **79**, 47-154.
10. F. A. Akgul, C. Gumus, A. O. Er, A. H. Farha, G. Akgul, Y. Ufuktepe and Z. Liu, *J. Alloy. Compd.*, 2013, **579**, 50-56.
11. L. Yu, D. Cai, H. Wang and M. M. Titirici, *RSC Advances*, 2013, **3**, 17281-17286.
12. L. Z. Liu, X. X. Li, X. L. Wu, X. T. Chen and P. K. Chu, *Appl. Phys. Lett.*, 2011, **98**. 133102.
13. J. S. Chen, M. F. Ng, H. B. Wu, L. Zhang and X. W. Lou, *Cryst. Eng. Comm.*, 2012, **14**, 5133-5136.
14. D. Wei, Y. Shen, M. Li, W. Liu, S. Gao, L. Jia, C. Han and B. Cui, *J. Nanomater.*, 2013, DOI: 10.1155/2013/761498.
15. C. Zhu, X. Xia, J. Liu, Z. Fan, D. Chao, H. Zhang and H. J. Fan, *Nano Energy*, 2014, **4**, 105-112.
16. J. Hu, Y. Bando, Q. Liu and D. Golberg, *Advanced Functional Materials*, 2003, **13**, 493-496.
17. E. J. H. Lee, C. Ribeiro, T. R. Giraldi, E. Longo, E. R. Leite and J. A. Varela, *Appl. Phys. Lett.*, 2004, **84**, 1745-1747.
18. L. Jiang, G. Sun, Z. Zhou, S. Sun, Q. Wang, S. Yan, H. Li, J. Tian, J. Guo, B. Zhou and Q. Xin, *J. Phys. Chem. B.*, 2005, **109**, 8774-8778.
19. A. Bouaine, N. Brihi, G. Schmerber, C. Ulhaq-Bouillet, S. Colis and A. Dinia, *J. Phys. Chem. C.*, 2007, **111**, 2924-2928.
20. H. Bastami and E. Taheri-Nassaj, *J. Alloy. Compd.*, 2010, **495**, 121-125.
21. S. Wu, C. Li, W. Wei, H. Wang, Y. Song, Y. Zhu and L. Lu, *J. Rare. Earth.*, 2010, **28**, 171-173.
22. N. S. Baik, G. Sakai, N. Miura and N. Yamazoe, *Journal of the American Ceramic Society*, 2000, **83**, 2983-2987.
23. A. Ayeshamariam, S. Ramalingam, M. Bououdina and M. Jayachandran, *Spectrochim. Acta. A.*, 2014, **118**, 1135-1143.
24. F. Gu, S. F. Wang, M. K. Lü, G. J. Zhou, D. Xu and D. R. Yuan, *J. Phys. Chem. B.*, 2004, **108**, 8119-8123.
25. A. J. Kenyon, *Progress in Quantum Electronics*, 2002, **26**, 225-284.
26. E. A. Morais, L. V. A. Scalvi, V. Geraldo, R. M. F. Scalvi, S. J. L. Ribeiro, C. V. Santilli and S. H. Pulcinelli, *J. Eur. Ceram. Soc.*, 2004, **24**, 1857-1860.
27. S. Chen, X. Zhao, H. Xie, J. Liu, L. Duan, X. Ba and J. Zhao, *Appl. Surf. Sci.*, 2012, **258**, 3255-3259.
28. L. P. Singh, M. N. Luwang and S. K. Srivastava, *New. J. Chem.*, 2014, **38**, 115-121.
29. E. A. Morais, L. V. A. Scalvi, A. Tabata, J. B. B. De Oliveira and S. J. L. Ribeiro, *J. Mater. Sci.*, 2008, **43**, 345-349.
30. E. A. d. Morais, L. V. A. Scalvi, A. A. Cavalheiro, A. Tabata and J. B. B. Oliveira, *J. Non-Cryst. Solids.*, 2008, **354**, 4840-4845.
31. S. Coffa, G. Franzò, F. Priolo, A. Polman and R. Serna, *Physical Review B*, 1994, **49**, 16313-16320.
32. H. Rinnert, P. Miska, M. Vergnat, G. Schmerber, S. Colis, A. Dinia, D. Muller, G. Ferblantier and A. Slaoui, *Appl. Phys. Lett.*, 2012, **100**, 101908.
33. http://www.rbnano.fr/.
34. A. L. Patterson, *Physical Review*, 1939, **56**, 978-982.
35. L. Z. Liu, T. H. Li, X. L. Wu, J. C. Shen and P. K. Chu, *J. Raman. Spectrosc.*, 2012, **43**, 1423-1426.
36. T. Hirata, K. Ishioka, M. Kitajima and H. Doi, *Physical Review B - Condensed Matter and Materials Physics*, 1996, **53**, 8442-8448.
37. J. X. Wang, D. F. Liu, X. Q. Yan, H. J. Yuan, L. J. Ci, Z. P. Zhou, Y. Gao, L. Song, L. F. Liu, W. Y. Zhou, G. Wang and S. S. Xie, *Solid. State. Commun.*, 2004, **130**, 89-94.
38. R. S. Katiyar, P. Dawson, M. M. Hargreave and G. R. Wilkinson, *Journal of Physics C: Solid State Physics*, 1971, **4**, 2421-2431.
39. F. Gervais and B. Piriou, *Physical Review B*, 1974, **10**, 1642-1654.
40. R. J. Betsch, H. L. Park and W. B. White, *Materials Research Bulletin*, 1991, **26**, 613-622.
41. L. Z. Liu, X. L. Wu, F. Gao, J. C. Shen, T. H. Li and P. K. Chu, *Solid. State. Commun.*, 2011, **151**, 811-814.
42. G. H. Dieke, *Spectra and Energy levels of Rare Earth Ions in Crystals*, Interscience publishers, New York, 1968.
43. S. Hüfner, *Optical Spectra of Transparent Rare Earth Compounds*, Academic Press, New York, San Fransisco, London, 1978.
44. P. Mulvaney, F. Grieser and D. Meisel, *Langmuir*, 1990, **6**, 567-572.
45. J. Jacquemin, *Le Journal de Physique Colloques*, 1974, **35**, C3-255-C253-260.
46. L. Dua and P. K. Biswas, *Chem. Phys. Lett.*, 2013, **572**, 66-72.
47. D. J. Norris, A. L. Efros, M. Rosen and M. G. Bawendi, *Physical Review B*, 1996, **53**, 16347-16354.
48. T. Kim, D. Lee and Y. Yoon, *Journal of Applied Physics*, 2000, **88**, 3759-3761.

49.   E. M. Wong and P. C. Searson, *Appl. Phys. Lett.*, 1999, **74**, 2939-2941.
50.   Y. Liu, W. Luo, H. Zhu and X. Chen, *J. Lumin.*, 2011, **131**, 415-422.